

Dual modification of hematite photoanode by Sn-doping and Nb₂O₅ layer for water oxidation

Tae Hwa Jeon ^a, Alok D. Bokare ^a, Dong Suk Han ^b, Ahmed Abdel-Wahab ^b, Hyunwoong Park ^{c,*}, Wonyong Choi ^{a,*}

^a School of Environmental Science and Engineering, Pohang University of Science and Technology (POSTECH), Pohang 37673, Republic of Korea

^b Chemical Engineering Program, Texas A&M University at Qatar, Education City, Doha 23874, Qatar

^c School of Energy Engineering, Kyungpook National University, Daegu 41566, Republic of Korea



ARTICLE INFO

Article history:

Received 13 May 2016

Received in revised form 8 July 2016

Accepted 26 August 2016

Available online 30 August 2016

Keywords:

Solar fuel

Photoelectrochemistry

Water splitting

Photoanode modification

Oxygen evolution

ABSTRACT

Porous hematite (α -Fe₂O₃) films doped with Sn(IV) and coated with an ultrathin (~2 nm thick) Nb₂O₅ passivation layer were synthesized, and the photoelectrochemical (PEC) water oxidation performance and durability of the hematite were examined in detail. As compared to hematite samples modified by either doping or passivation, dual-modified hematite exhibited a promising PEC water oxidation performance under AM 1.5 irradiation. A stable photocurrent was maintained under prolonged irradiation over 24 h, while O₂ was produced from water with a Faradaic efficiency of over 80% without showing any sign of deactivation. This performance and durability could be decoupled into separate effects of Sn doping and Nb₂O₅ layer via in-depth surface characterization and electrochemical analyses. Sn doping increased the donor density (N_d) of bare hematite by a factor of 20 and significantly improved its conductivity, leading to enhanced charge transfer efficiency. The Nb₂O₅ layer exerted an effect similar to Sn doping because of the diffusion of a fraction of Nb(V) into the hematite lattice during the annealing process at 700 °C. The primary effect of the Nb₂O₅ layer is to passivate the hematite surface and make the surface more reactive toward the oxygen evolution through water oxidation. These effects are synergistically combined in the dual-modified hematite electrode.

© 2016 Elsevier B.V. All rights reserved.

1. Introduction

Hematite (α -Fe₂O₃) is a promising semiconductor for water oxidation owing to its suitable optical bandgap ($E_g \sim 2.2$ eV), high thermal stability, natural abundance, and nontoxicity [1–3]. Nevertheless, its actual photoelectrochemical (PEC) efficiency was reported to be significantly lower than the optical limit (~15%) [1–3], primarily due to the inherently sluggish charge transfer kinetics arising from poor conductivity ($\sim 10\text{--}14 \Omega^{-1} \text{cm}^{-1}$) [4] and low mobility of charge carriers ($\sim 10^{-2} \text{ cm}^2 \text{V}^{-1} \text{s}^{-1}$) [5]. In addition, the low catalytic efficiency (i.e., inefficient charge injection) of the hematite surface significantly decreased the Faradaic efficiency for water oxidation. Many efforts have been made to overcome these challenges, including element-doping [6–8] and surface passivation [9–11].

Doping with high-valent ions (e.g., Sn⁴⁺ and Ti⁴⁺) is a major approach to improve electrical conductivity, which is related to

charge transfer kinetics. For example, an incorporated Sn⁴⁺ ion provides an extra electron to the hematite lattice, increasing its donor density (N_d) [12,13] and thereby charge transfer efficiency by 50% [14]. However, recent studies disclosed the occurrence of Sn thermal diffusion to hematite films from the underlying transparent conducting oxide substrates (TCO; e.g., fluorine-doped SnO₂ thin film (FTO) on soda lime silica glass) during annealing [15,16]. Although high-temperature annealing should improve the crystallinity of hematite, it caused the deformation of the TCO substrate and led to decreased electrical conductivity of the substrates. This trade-off between the improvement of over-layered hematite performance by unintentional Sn doping and the deactivation of under-layered TCO by Sn-leaching makes the evaluation of the actual effect of Sn(IV) doping on the charge transfer behavior complicated.

Even though charge transfer is facilitated, the sluggish injection of surface charge carriers into the solution limits the Faradaic efficiency [13,17]. The hematite surface possesses a number of surface states responsible for charge carrier recombination. To address this challenge, the hematite surface was often coated with ultrathin (0.1–10 nm) oxide layers, including Al₂O₃, TiO₂, SnO₂, etc.

* Corresponding authors.

E-mail addresses: hwp@knu.ac.kr (H. Park), wchoi@postech.edu (W. Choi).

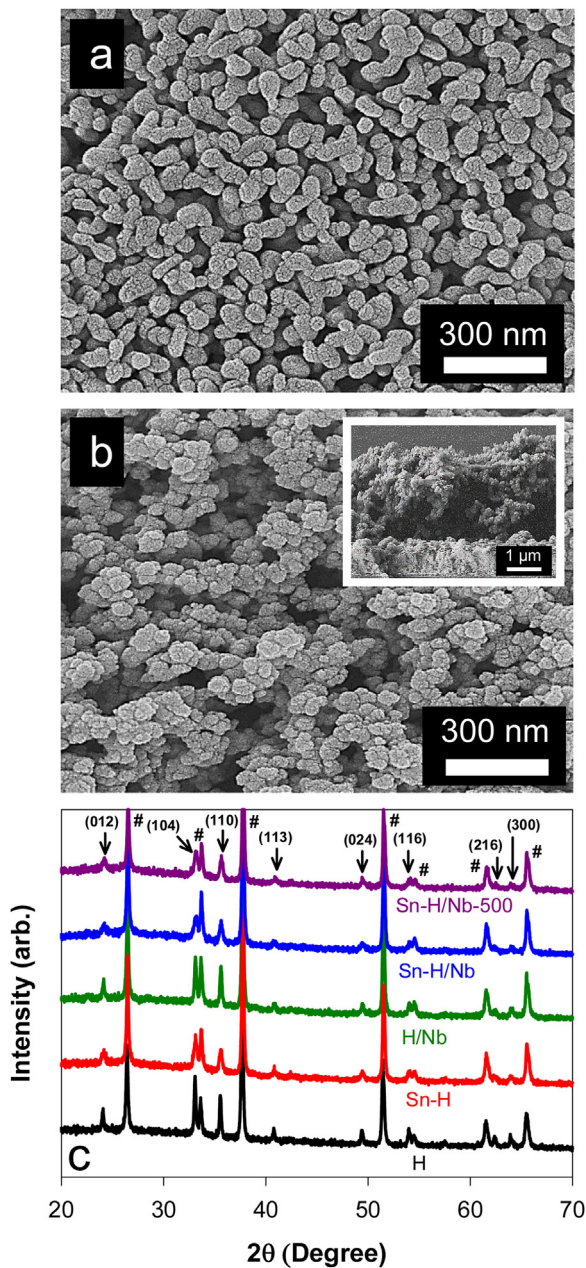


Fig. 1. SEM images of (a) bare hematite (denoted H) and (b) hematite modified by Sn doping and Nb₂O₅ coating (denoted H-Sn/Nb). The inset shows a cross-sectional view of the H-Sn/Nb film. (c) XRD patterns of bare and modified hematite samples. H: hematite, Sn-H: Sn-doped hematite, H/Nb: hematite coated with Nb₂O₅ layer, Sn-H/Nb: hematite doped with Sn and coated with Nb₂O₅ layer, Sn-H/Nb-500: Sn-H/Nb annealed at 500 °C. Unless otherwise specified, the final annealing temperature is 700 °C. All iron oxide peaks are assigned to crystalline hematite phases (JCPDS No. 01-089-0596), while # represents the peaks of crystalline SnO₂ originating from FTO substrate (JCPDS No. 01-077-0452).

[18–20]. These nanometer-thick oxide layers effectively passivated the surface states and led to prompt hole injection, consequently reducing photocorrosion and inhibiting charge recombination [10]. However, metal ions of the surface oxide layers can diffuse into the hematite interior during annealing [21–23], unintentionally doping the bare hematite. Therefore, the surface passivation process exerts the same effect as donor-doping, and the obtained hematite is virtually “doped” and “passivated”.

With this in mind, this study attempted to synthesize highly efficient, durable hematite for PEC water oxidation. To achieve this, we designed a straightforward yet highly reliable strategy of dual

modification: doping with Sn(IV) and passivation with Nb₂O₅ layer. Sn⁴⁺ is one of the widely used hematite dopants [1,3,14]. A thin layer of Nb₂O₅ was reported to play a role in passivating TiO₂ [24–26], while Nb(V) was used as a dopant for hematite [27,28]. Bare and Sn(IV)-doped hematite films were grown in situ on an FTO electrode by electrodeposition and annealed at 700 °C. Subsequently, a Nb₂O₅ layer (~2 nm thick) was uniformly coated on the hematite surface by precursor solution casting and post-annealing processes. The surface of the dual-modified hematite films was systematically characterized with various analytical tools. In addition, detailed electrochemical and photoelectrochemical analyses were performed to examine the effects of dual modification and to gain further insights on charge transfer and injection behaviors.

2. Experimental

2.1. Synthesis of bare and modified hematite film electrodes

Hematite (denoted H) electrodes were prepared via an electrochemical deposition method reported previously [29,30]. In brief, an FTO glass substrate (F:SnO₂ Pilkington, 15 Ω/square, 1.0 cm × 3.0 cm, sequentially rinsed with acetone, ethanol, and distilled water), an Ag/AgCl electrode (3 mol L⁻¹ KCl), and a Pt wire were employed as a working, a reference, and a counter electrode, respectively. They were placed in the aqueous precursor solution containing FeCl₃·6H₂O (5 mM, Sigma Aldrich), NaF (5 mM, Samchun), NaCl (0.1 M, Samchun), and H₂O₂ (1 M, Samchun). Subsequently, potentials were swept from –0.52 to +0.41 V (vs. Ag/AgCl) at a scan rate of 0.1 V s⁻¹ for 100 cycles using a potentiostat/galvanostat (Versastat 3-400, Ivium Technologies) to deposit iron oxides. For Sn(IV)-doped hematite (Sn-Fe₂O₃; denoted Sn-H), SnCl₄·5H₂O (Sigma Aldrich) was added to the precursor solution at Sn/Fe molar ratios between 1% and 6.25%, followed by the same deposition procedure. After rinsing with deionized water and drying at room temperature, the bare and Sn-doped iron oxide samples were sequentially annealed at 600 °C for 4 h with a ramping rate of 2 °C min⁻¹ (pre-annealing) and at 700 °C for 1 h (post-annealing). For surface coating with Nb₂O₅, 6 μL of Nb(V) solution (NbCl₅, Sigma Aldrich, dissolved in ethanol) at Nb concentrations between 30 and 150 mM were drop-cast on the pre-annealed hematite samples (i.e., H and Sn-H). After drying in air for 1 h, the Nb-treated samples (H and Sn-H) were annealed at 700 °C for 1 h to convert Nb(V) ions into Nb₂O₅ (denoted H/Nb and Sn-H/Nb, respectively) [23]. To examine the effect of Nb(V) diffusion, the Nb(V) solution was drop-cast on Sn-Fe₂O₃ (pre- and post-annealed) and annealed at 500 °C once again (denoted Sn-H/Nb-500). Accordingly, all samples (H, Sn-H, H/Nb, Sn-H/Nb) were obtained using the same annealing sequence (600 and 700 °C), whereas Sn-H/Nb-500 underwent three annealing cycles: 600, 700, and 500 °C. If necessary, the as-prepared samples were further treated with cobalt ions (Co²⁺) by immersion in the aqueous solution of 0.1 M Co(NO₃)₂ for 1 min, rinsing with deionized water, and drying in air [31,32]. The loaded cobalt species did not display crystalline structures, whereas they were simply adsorbed on the surface in the states of Co(OH)₂ and/or CoO (Fig. S1 in Supplementary material).

2.2. Electrochemical and photoelectrochemical measurements

The as-synthesized hematite working electrode, an Ag/AgCl reference electrode, and a Pt wire counter electrode were immersed in aqueous KOH solution (0.1 M; pH ~13) pre-purged with Ar gas for 15 min, and the potentials of the working electrode were swept from –0.5 to +0.8 V (vs. Ag/AgCl) at a scan rate of 0.02 V s⁻¹ by a potentiostat (Versastat 3-400) in the dark or under irra-

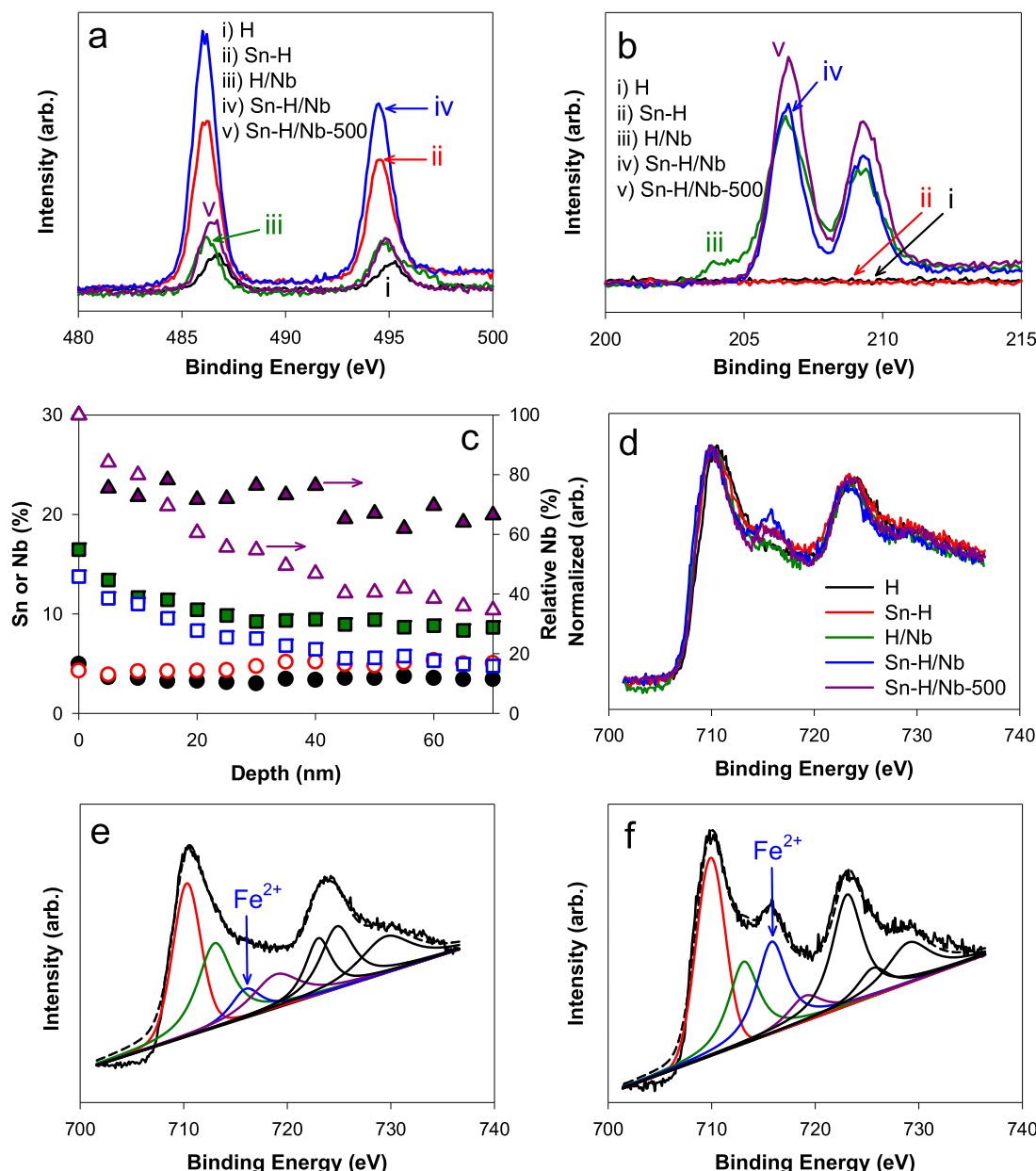


Fig. 2. XPS spectra of as-synthesized samples for (a) Sn 3d and (b) Nb 3d bands. (c) XPS depth profiles of as-synthesized samples for Sn (filled circles: Sn-H/Nb, open circles: Sn-H/Nb-500) and Nb (filled squares: Sn-H/Nb, open squares: Sn-H/Nb-500). Relative niobium contents ($\text{Nb}/(\text{Nb} + \text{Fe}) \times 100\%$) were compared between Sn-H/Nb (filled triangles) and Sn-H/Nb-500 (open triangles) as a function of depth. (d) XPS Fe 2p bands of as-synthesized samples. Resolved Fe 2p bands of (e) H and (f) Sn-H/Nb. See Fig. S4 for assignment of the sub-bands.

Table 1
Summary of physicochemical and (photo)electrochemical properties of samples.

Sample ^a	Size (nm) ^b	Fraction (%) ^c			N_d ($\times 10^{18} \text{ cm}^{-3}$) ^d	R_{ct} (k Ω) ^e	R_{bulk} (k Ω) ^e	E_{on} (V) ^f	E_{fb} (V) ^f	η_{sep} (%) ^g	η_{inj} (%) ^g
		Sn	Nb	Fe^{2+}							
H	50	3.6	–	6.6	0.12	22.88	10.74	1.54	0.45	2.2	14.6
Sn-H	40	12.6	–	13.6	2.35	3.17	1.14	1.19	0.38	5.4	18.6
H/Nb	60	6.8	35.9	8.6	2.82	4.94	2.17	1.15	0.43	2.6	41.6
Sn-H/Nb	50	12.4	31.7	20.7	10.1	1.19	0.97	1.11	0.34	4.2	57.8
Sn-H/Nb-500	50	10.8	37.4	13.9	2.20	6.75	2.14	1.17	0.42	5.4	44.2

^a Unless otherwise specified, all samples were pre-annealed at 600 °C and post-annealed at 700 °C. H: hematite, Sn-H: Sn-doped hematite, H/Nb: hematite coated with Nb_2O_5 layer, Sn-H/Nb: hematite doped with Sn and coated with Nb_2O_5 layer, Sn-H/Nb-500: the same as Sn-H/Nb except for post-annealing at 500 °C.

^b Estimated from SEM analysis.

^c $M/(M + \text{Fe}) \times 100\%$ where $M = \text{Sn}$ or Nb . Fe^{2+} fraction = $\text{Fe}^{2+}/(\text{Fe}^{2+} + \text{Fe}^{3+}) \times 100\%$.

^d Donor density.

^e R_{ct} : Solid/solution interfacial resistance, R_{bulk} : Solid bulk resistance.

^f E_{on} : Onset potential vs. RHE, E_{fb} : flat band potential vs. RHE.

^g η_{sep} : Charge separation efficiency, η_{inj} : Charge injection efficiency. Both were estimated at $E = 1.23 \text{ V}$ vs. RHE.

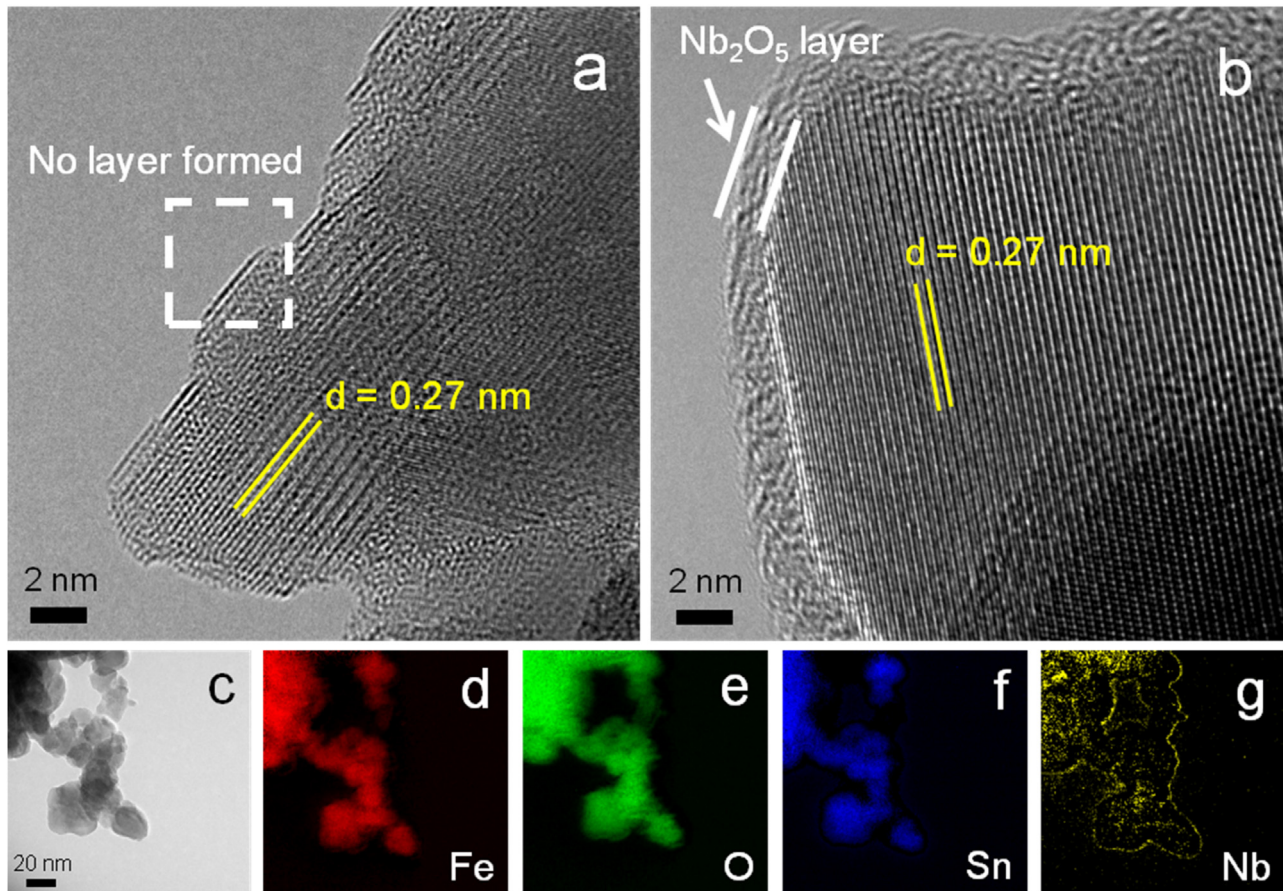


Fig. 3. HR-TEM images of (a) Sn-H and (b) Sn-H/Nb. (c) TEM image of Sn-H/Nb and EELS elemental mappings for (d) Fe, (e) O, (f) Sn, and (g) Nb.

diation. If necessary, a constant potential (+0.27 V vs. Ag/AgCl) was applied to the working electrode. The back (i.e., FTO) side of the hematite electrode (area: 0.3 cm × 0.35 cm) was irradiated by a 150-W Xenon arc lamp (ABET Tech.) equipped with an air mass (AM) 1.5G filter (100 mW cm⁻²). The incident photon-to-current efficiency (IPCE) was estimated in 0.1 M KOH with the same three-electrode system using a 300 W-Xenon lamp (Newport Oriel). Monochromatic light was produced by a CS 130 monochromator with a 10 nm-bandpass, and the output power was measured with a silicon photodiode detector (Newport) [33]. The IPCE was then calculated from $(1240 \times J_{ph}) \times 100 / (P_{light} \times \lambda)$, where J_{ph} (mA/cm²), P_{light} (mW/cm²), and λ (nm) refer to the photocurrent density at +0.27 V (vs. Ag/AgCl), photon flux, and wavelength, respectively. For Mott-Schottky analysis, various potentials from -0.96 to -0.06 V (vs. Ag/AgCl) were applied at a frequency of 1 kHz in the dark. Electrochemical impedance analysis (EIS) was performed at a potential of +0.27 V (vs. Ag/AgCl) with an AC voltage of 50 mV and a frequency range of 1 MHz to 0.01 Hz in the dark and under irradiation. Unless otherwise mentioned, the values of potentials relate to a reversible hydrogen electrode (RHE) by the following equation: $V_{RHE} = V_{Ag/AgCl} + 0.197 + 0.059 \times pH$. For gas (O_2 and H_2) evolution measurements, the electrolyte was purged with Ar for 30 min, and a constant potential of +0.27 V (vs. Ag/AgCl) (corresponding to +1.23 V vs. RHE) was applied to the hematite electrode prior to irradiation. While irradiating, 100 μ L of headspace gas was intermittently withdrawn from the reactor with a syringe (Hamilton 81030) and analyzed using a gas chromatograph (GC, HP6890A) equipped with a thermal conductivity detector (TCD) and a 5 \AA molecular sieve column.

2.3. Surface characterization

The morphology of bare and modified hematite samples was characterized using field-emission scanning electron microscopy (FE-SEM; JEOL JSM-7401F), high-resolution transmission electron microscopy (HR-TEM; JEM-2100F), and electron energy loss spectroscopy (EELS) analysis using a Cs-corrected line at the National Institute for Nanomaterials Technology (Pohang, Korea). X-ray diffraction (XRD) patterns were measured with Cu $K\alpha$ radiation (MAC Science, M18XHF). UV-vis absorption spectra were recorded on a spectrophotometer (Shimadzu UV-2401PC). The surface elemental composition was analyzed by X-ray photoelectron spectroscopy (XPS; Theta Probe AR-XPS System) using monochromated Al $K\alpha$ radiation as an X-ray source (1486.6 eV, Busan Center, KBSI, Korea).

3. Results and discussion

3.1. Characterization of hematite films

The SEM images of bare (i.e., non-modified) hematite (H) films show that spherical particles of uniform size (~50 nm in diameter) were formed and are well interconnected (Fig. 1a). The particle sizes of Sn-doped (Sn-H; Fig. S2a), Nb_2O_5 -coated (H/Nb; Fig. S2b), and dual-modified hematite (Sn-H/Nb; Figs. 1b and S2c) were similar to that of bare hematite. The film thickness of the dual-modified sample was ~3 μ m, being locally variable owing to porous structure (Fig. 1b inset). The as-synthesized samples exhibited typical peaks assigned to crystalline hematite ($2\theta = 24.14^\circ, 33.15^\circ, 35.61^\circ, 40.86^\circ, 49.48^\circ, 54.09^\circ, 62.45^\circ$, and 63.99° for (012), (104), (110),

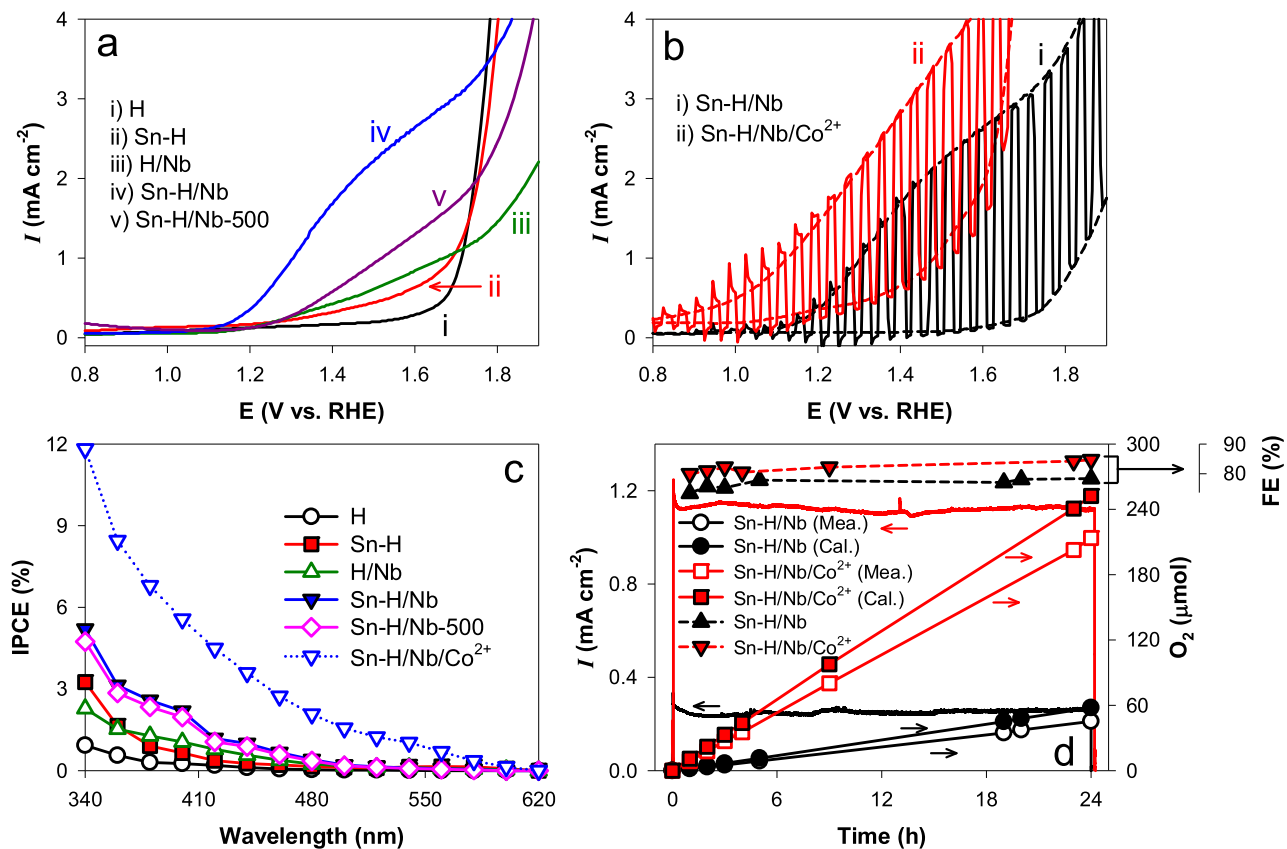


Fig. 4. (a) Linear sweep voltammograms (LSVs) of bare and modified samples in aqueous KOH solution (0.1 M; pH 13) pre-purged with Ar under AM 1.5 light (100 mW cm⁻²). (b) Chopped LSVs of Sn-H/Nb and Co²⁺-treated Sn-H/Nb. See the experimental section for detail. (c) IPCE values of samples at $E = 1.23$ V vs. RHE. (d) Time-profiled photocurrent generation for Sn-H/Nb and Co²⁺-treated Sn-H/Nb (black and red lines, respectively) and simultaneous O₂ production. The Faradaic efficiencies for O₂ production (right offset y-axis) were estimated by comparing the measured (mea.) and calculated (cal.) O₂ quantities. Unless otherwise specified, the experimental conditions were identical to those in Fig. 4a. (For interpretation of the references to colour in this figure legend, the reader is referred to the web version of this article.)

(113), (024), (116), (214), and (300) planes, respectively; JCPDS card no. 01-089-0596; see Fig. 1c). The peak intensities (e.g., (104) and (110) planes) were slightly decreased by Sn doping or Nb₂O₅ coating, whereas no additional peaks attributable to SnO₂ or Nb₂O₅ were found. Typically, the minor element-oriented peaks were not observed. Nonetheless, the possible formation of SnO₂ cannot be excluded, since the peak of crystalline SnO₂, if present, can overlap with SnO₂ peaks of the FTO substrate. On the other hand, the absence of crystalline Nb₂O₅ peaks was obvious, presumably due to the thinness of the layer. It is of note that the XRD peak intensity of hematite was slightly variable among samples because of porous morphology, whereas that of FTO was nearly invariable.

XPS analyses of the samples were further performed to obtain evidence for Sn and Nb existence and gain knowledge on the chemical states of Fe (Fig. 2; see Fig. S3 for survey spectra). Sn 3d peaks were found not only in Sn-doped hematite samples (Sn/Fe ratios of 12.6, 12.4, and 10.8% for Sn-H, Sn-H/Nb, and Sn-H/Nb-500, respectively), but also in bare ones (Sn/Fe ratios of 3.6 and 6.8% for H and H/Nb, respectively), owing to the diffusion of Sn(IV) (i.e., self-doping) from the FTO substrate during annealing (Fig. 2a and Table 1). On the other hand, Nb 3d peaks were found only in Nb(V)-treated samples (Nb/Fe ratios of 35.9, 31.7, and 37.4% for H/Nb, Sn-H/Nb, and Sn-H/Nb-500, respectively) (Fig. 2b and Table 1). It is notable that even though the Nb(V) precursor solution is drop-cast on the pre-annealed (i.e., crystallized) hematite particles, a fraction of Nb(V) appears to diffuse into hematite particles during post-annealing at 700 °C. An XPS depth profile shows that the Sn atomic content was insignificantly variable (<5%) throughout 70 nm depth within the outermost hematite surface (Fig. 2c). This distribution

pattern suggests that Sn was uniformly doped, although quantifying the contribution of self-doping was rather difficult. Meanwhile, the Nb atomic content decreased from 16% at the depth of 0 nm to ~9% at the depth of 70 nm in Sn-H/Nb (~43% decrease), whereas it decreased to ~5% at the depth of 70 nm in Sn-H/Nb-500 (~67% decrease). This confirms the speculation that the thermally induced Nb diffusion into the hematite interior is retarded by reducing the annealing temperature from 700 to 500 °C.

In addition, bare and modified hematite samples showed two characteristic Fe 2p bands (~710 and ~725 eV for Fe 2p_{3/2} and Fe 2p_{1/2}, respectively, Fig. 2d). It is noteworthy that Fe(II) bands at ~716 eV were observed for most samples, with the following Fe(II)/Fe(III) elemental ratios: Sn-H/Nb (20.7%) > Sn-H/Nb-500 (13.9%) > Sn-H (13.6%) > H/Nb (8.6%) > H (6.6%) (Figs. 2e, 2f, S4, and Table 1). The fact that the Fe(II) band was found even for bare hematite suggests the occurrence of thermal diffusion of high-valent Sn(IV) from the FTO substrate into the hematite lattice, followed by substitution and/or occupation of vacant interstitial sites [34] and reduction of Fe³⁺ to Fe²⁺ to maintain overall charge neutrality [35–38]. Accordingly, Sn-H (i.e., an intentionally Sn-doped sample) exhibited a higher level of Fe(II) compared to the self-doped sample (i.e., bare hematite). The H/Nb sample showed an increased Fe(II) fraction as well, due to partial diffusion of drop-cast Nb into the hematite lattice during post-annealing (Fig. S4 and Table 1). Compared to Sn-H, the lower Fe(II) content of H/Nb was ascribed to the fact that Sn diffusion occurs twice during pre-annealing and post-annealing, whereas the diffusion of Nb occurs only once in the post-annealing step. The dual-modified sample (Sn-H/Nb) showed the highest Fe(II) fraction (20.7%) due to the

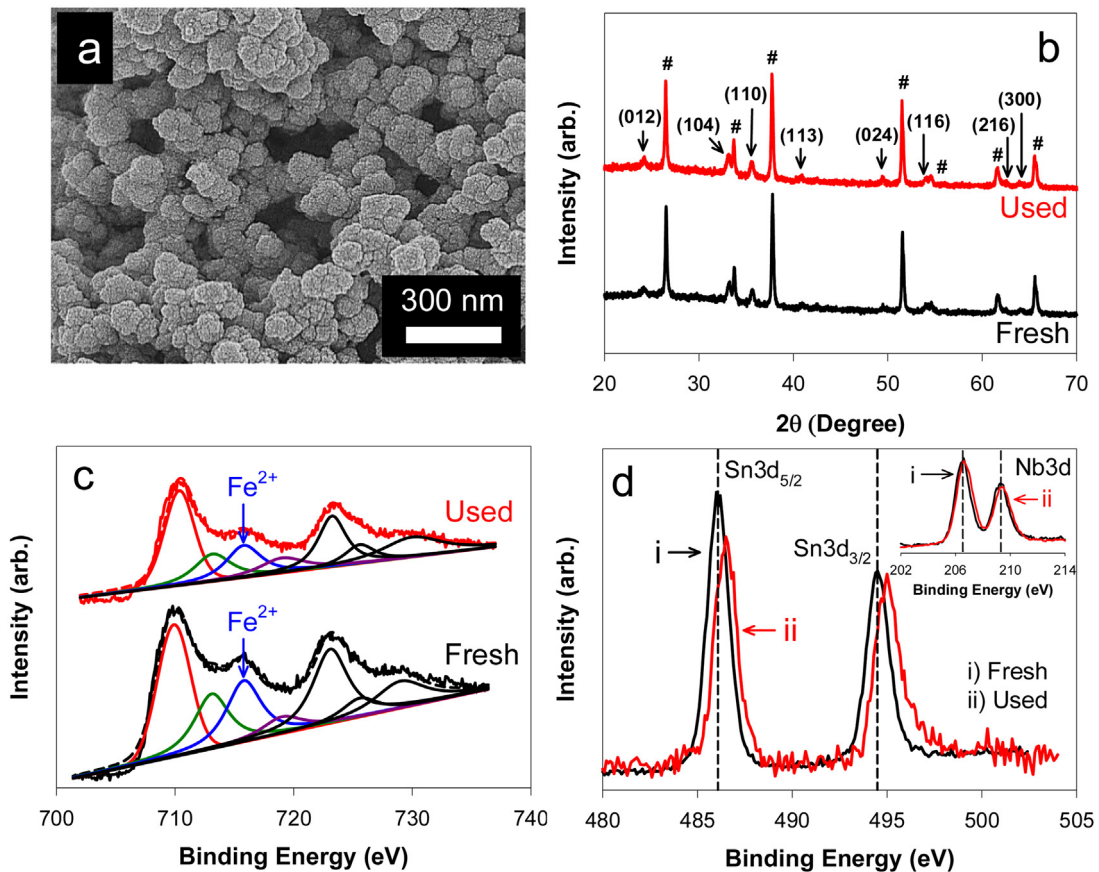


Fig. 5. (a) SEM image of a Sn-H/Nb sample used for 24 h (see Fig. 4d). Comparison of as-fabricated Sn-H/Nb samples used for 24 h: (b) XRD (see Fig. 1c for symbol “#” and JCPDS numbers), (c) XPS Fe 2p bands (as-obtained and resolved), and (d) XPS Sn 3d bands (inset: Nb 3d bands).

combined effect of Sn(IV) and Nb(V) diffusion (Fig. 2f). The similar Fe(II) content of Sn-H and Sn-H/Nb-500 further indicates that thermal diffusion of Nb(V) was inhibited at an annealing temperature of 500 °C.

TEM images of Sn-doped hematite samples without and with Nb_2O_5 treatment (Sn-H and Sn-H/Nb, respectively) were obtained (Fig. 3). The lattice fringe spacing of both samples was 0.27 nm, corresponding to the (104) lattice plane of hematite. Compared to Sn-H, Sn-H/Nb clearly showed a ~2-nm-thick amorphous thin adlayer, which was uniformly coated on hematite particles (Fig. 3a and b). EELS elemental mappings of the Sn-H/Nb sample further indicate that Fe, O, and Sn were uniformly distributed in the entire particle aggregates, and their spatial distribution patterns were nearly the same (Figs. 3c–f). On the other hand, Nb was found predominantly on the aggregate edges, suggesting that the 2 nm thick layer was due to Nb_2O_5 (Fig. 3g).

3.2. Photoelectrochemical performance and durability of modified hematite

The photoelectrochemical (PEC) behavior of bare and modified hematite was compared in alkaline solution (0.1 M KOH; pH ~13) under irradiation by AM 1.5 light (100 mW cm^{-2}). As shown in Fig. 4a, bare hematite exhibited an onset potential (E_{on}) of ~1.5 V, with Sn doping (at 5%) and Nb_2O_5 treatment (at 100 mM) shifting E_{on} by about -0.35 and -0.39 V, respectively. Despite these shifts, the magnitudes of photocurrents for Sn-H were not significant (e.g., $I_{\text{ph}} < 0.15 \text{ mA cm}^{-2}$) at the oxygen evolution potential (1.23 V). Other Sn doping levels (1.25–6.25%) were examined as well (Fig. S6a). Although an optimum level of Sn doping existed,

its effect on the magnitudes of photocurrent (at 1.23 and 1.4 V) was marginal. On the other hand, Sn-H/Nb showed E_{on} of ~1.1 V and generated a photocurrent of 0.51 mA cm^{-2} at 1.23 V (Fig. 4a), with this enhancement resulting mostly from the effect of Nb_2O_5 (Fig. S4b). Increases in potentials of Sn-H/Nb by 0.2 and 0.4 V (i.e., $E = 1.43$ and 1.63 V, respectively) markedly increased the respective photocurrents to 1.85 and 2.76 mA cm^{-2} . These values were greater than the sums of Sn-H and H/Nb photocurrents at respective potentials ($E = 1.23$, 1.43 , and 1.63 V). To further improve the PEC performance, cobalt ions (Co^{2+}) were drop-cast on the dual-modified hematite. Upon Co^{2+} treatment, E_{on} was further shifted to ~0.7 V, while a photocurrent of $\sim 2 \text{ mA cm}^{-2}$ was generated at 1.23 V (Fig. 4b). In alkaline solution, the adsorbed Co^{2+} is in situ transformed into cobalt hydroxides (i.e., Co(OH)_2), which play the role of co-catalysts capable of mediating hole transfer on hematite surface (e.g., $\text{Co}^{2+} + 2 \text{ h}^+ \rightarrow \text{Co}^{4+}$; $\text{Co}^{4+} + \text{H}_2\text{O} \rightarrow \text{Co}^{2+} + 1/2\text{O}_2 + 2\text{H}^+$) [31]. The cobalt-treated hematite generated current at $E > \sim 1.1$ V in the absence of irradiation, presumably due to an increase in conductivity. The effects of surface modification were further compared in terms of IPCE values (Fig. 4c). Bare hematite exhibited poor IPCE values of less than 1% in the range of $\lambda \geq 340$ nm, whereas the values for dual-modified hematite were ~5 and ~1% at $\lambda = 340$ and 420 nm, respectively. Co^{2+} treatment further improved the IPCE values of dual-modified hematite to 12 and ~4.5% at $\lambda = 340$ and 420 nm, respectively.

The capability of dual-modified hematite electrodes for oxygen evolution was examined at $E = 1.23$ V under AM 1.5 light irradiation (Fig. 4d). A stable photocurrent of $\sim 0.25 \text{ mA cm}^{-2}$ flowed over 24 h without any sign of deactivation, while O_2 was continuously produced at a rate of $\sim 1.88 \mu\text{mol h}^{-1}$. These performance and dura-

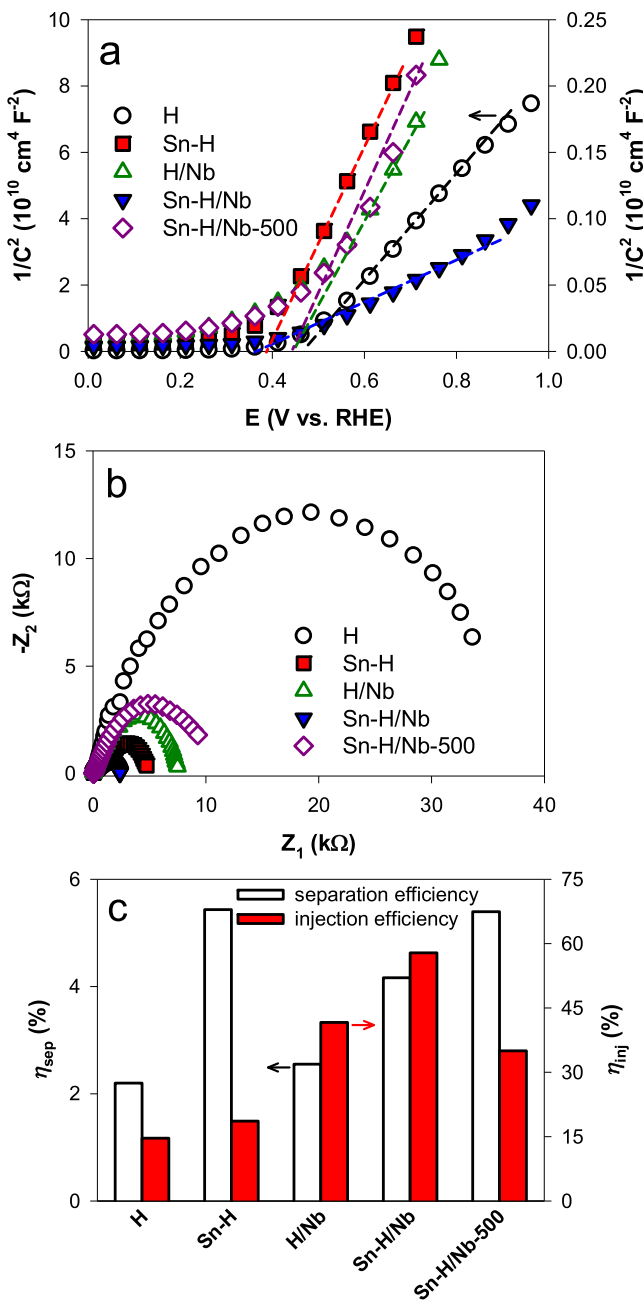


Fig. 6. (a) Mott-Schottky plots at a fixed frequency of 1 kHz in aqueous KOH solution (0.1 M; pH 13) purged with Ar. (b) Nyquist plots at $E = 1.23$ V vs. RHE in the aforementioned electrolyte. (c) Charge separation (open bar, left axis) and injection efficiencies (filled bar, right axis) of samples at 1.23 V vs. RHE in the aforementioned electrolyte.

bility are quite comparable to those in previous reports (Table S1). In the same set of experiments, H_2 was stoichiometrically produced at a rate of $\sim 3.87 \mu\text{mol h}^{-1}$ ($\text{H}_2/\text{O}_2 = 2/1$, Fig. S8). The Faradaic efficiencies for O_2 evolution were maintained at $\sim 80\%$ during the whole irradiation period, indicating that the H-Sn/Nb samples have high catalytic activity. After Co^{2+} treatment, a more than four-fold stable photocurrent ($\sim 1.1 \text{ mA cm}^{-2}$) flowed over 24 h, and linear O_2 production at $\sim 8.90 \mu\text{mol h}^{-1}$ was obtained. The Faradaic efficiencies for O_2 and H_2 evolutions were $\sim 85\%$, with showing no sign of deactivation after 24 h. The role of Co^{2+} is to facilitate the kinetically sluggish hole transfer, leading to an increase in photocurrent [31,32,39].

In addition, the durability of dual-modified hematite was examined in depth in terms of surface states after the continuous photoelectrochemical reaction for 24 h. The overall morphology appeared to be the same as that of the as-synthesized sample (Fig. 1b vs. Fig. 5a), whereas the particle size became slightly larger (~ 100 nm). Typically, oxide semiconductors undergo interparticle aggregation during photo-processes, leading to an increase in particle size [40]. XRD patterns further indicate that the hematite crystalline structure was not changed after 24 h (JCPDS No. 01-089-0596) (Fig. 5b). On the other hand, comparison of Fe 2p XPS bands clearly shows that the fraction of Fe^{2+} was reduced from 20.7 to 15.8%, which is attributed to the oxidation of Fe^{2+} to Fe^{3+} by holes (Fig. 5c). This Fe^{2+} oxidation influences the pre-established charge neutrality, leading to the diffusion of substituted or interstitial Sn(IV) to the surface. The XPS binding energy of the Sn 3d band was shifted by ~ 0.5 eV after the 24 h-reaction (Fig. 5d), confirming the change in Sn(IV) states (e.g., ionic Sn(IV) to SnO_2) [41]. In contrast, the binding energy of Nb 3d was insignificantly shifted, indicating the stability of the surface-passivating Nb_2O_5 layer (Fig. 5d inset). Neither Sn nor Nb species are found in the electrolyte solution used for the durability test.

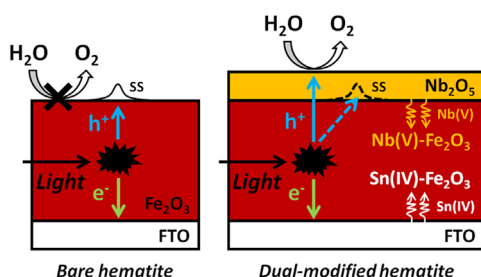
3.3. Origin of the dual modification effects

The effect of surface modification on the bandgap of hematite was found to be insignificant (Fig. S9). Even if the bandgap is altered, its actual contribution should be minimal, since the IPCE onsets of bare and modified electrodes (see Fig. 4c) were nearly the same (~ 540 nm). Considering the high-valence states of Sn(IV) and Nb(V), their primary role was presumed to be the donation of electrons to hematite. To examine this possibility, Mott-Schottky analysis was carried out with bare and modified hematite electrodes (Fig. 6a), and the donor densities (N_d) and flat band potentials (E_{fb}) were estimated by the following equation:

$$\frac{1}{C_{SC}^2} = \frac{2}{q\epsilon\epsilon_0 N_d} \left(E - E_{fb} - \frac{kT}{q} \right)$$

where C_{SC} , q , ϵ , ϵ_0 , N_d , E , E_{fb} , k , and T refer to space charge capacitance (F cm^{-2}), elementary charge ($1.602 \times 10^{-19} \text{ C}$), relative dielectric constant of hematite (32), permittivity of vacuum ($8.85 \times 10^{-12} \text{ N}^{-1} \text{ C}^2 \text{ m}^{-2}$), donor density (cm^{-3}), applied potential (V), flatband potential (V), Boltzmann's constant ($1.38 \times 10^{-23} \text{ J K}^{-1}$), and absolute temperature (K), respectively. N_d for $\text{Sn}-\text{Fe}_2\text{O}_3$ was estimated to be $\sim 2.35 \times 10^{18} \text{ cm}^{-3}$, which is ~ 20 times higher than that of bare hematite (Table 1). Coupling of the Nb_2O_5 layer induced a similar effect to Sn doping, due to the doping of a fraction of Nb(V) during post-annealing. Accordingly, dual modification exerted a combined effect with two orders of magnitude greater N_d compared to bare hematite. Inhibition of Nb(V) doping by reducing the post-annealing temperature led to an N_d value similar to that of $\text{Sn}-\text{Fe}_2\text{O}_3$, suggesting that a fraction of Nb(V) was actually doped, while the remaining Nb(V) was converted to Nb_2O_5 during high-temperature annealing. The increases in N_d should intensify the n -type character of hematite, leading to upward shifts of the Fermi level. In accord with the speculation, the E_{fb} of the Sn-H/Nb sample was ~ 0.34 V, which is more negative than that of bare hematite by 0.1 V (Table 1). This shift is attributed primarily to the effect of Sn doping (Scheme 1).

Increased N_d should further improve electrical conductivity while reducing electrode bulk resistance (R_{bulk}) and charge transfer resistance (R_{ct}). EIS analyses of bare and modified hematite were conducted to estimate R_{bulk} and R_{ct} and examine the charge transfer kinetics at the solid/solution interface and in the bulk semiconductor (Fig. 6b; see Fig. S10 for the corresponding electrical circuit) [42]. As shown in Nyquist plots, R_{bulk} and R_{ct} of bare hematite



Scheme 1. Schematic of charge transfer processes at bare (left) and dual-modified (right) hematite electrodes under illumination. Dashed lines represent suppressed processes. SS: surface trap states. Note that diffusion of Sn(IV) and Nb(V) occurs in the hematite electrode from FTO and Nb₂O₅, respectively (zigzag arrow), during high temperature annealing (700 °C).

(10.74 kΩ and 22.88 kΩ, respectively) were ~10-fold and ~20-fold decreased by dual modification. These two parameters are associated with interparticle resistance and the solid/solution interfacial resistance, respectively, and influence the overall PEC efficiencies. This combined effect can be decoupled into charge separation efficiency (η_{sep}) within the hematite film and charge injection (η_{inj}) at the hematite/solution interface, using an electrochemical technique reported previously (see Fig. S11 for the analytical method) [17,43,44]. As shown in Fig. 6c and summarized in Table 1, bare hematite exhibited poor η_{sep} of only ~2% due to low majority carrier conductivity and short diffusion length of the minority carrier. Sn doping improved η_{sep} to ~5%, with the effect of Nb₂O₅ layer being marginal, leading to the value of η_{sep} for dual modified hematite being as low as ~4%, which is significantly lower than the values reported in literature [17]. On the other hand, η_{inj} was increased from ~15 to ~42% by Nb₂O₅, and to ~58% by dual modification, whereas the effect of Sn doping on η_{inj} was insignificant. Accordingly, the primary effects of Sn doping and Nb₂O₅ layer are to increase η_{sep} and η_{inj} , respectively. The same η_{sep} value for Sn-H and Sn-H/Nb-500 further confirms the role of Sn doping, while the similar η_{inj} values for H/Nb and Sn-H/Nb-500 samples imply that the presence of the Nb₂O₅ layer on hematite is critical in facilitating the interfacial charge transfer for water oxidation.

4. Conclusions

This study demonstrates that dual modification of hematite by donor doping and surface passivation is very effective in improving its PEC performance and securing the durability. The primary effect of Sn(IV) is to increase donor density and facilitate charge transfer, while the effect of the ~2-nm-thick Nb₂O₅ layer is to improve charge injection efficiency and facilitate the oxygen evolution reaction. These two effects are synergistically combined in the PEC process with dual-modified hematite electrodes. As compared to Nb₂O₅, the effect of Sn doping is relatively insignificant, since even bare hematite is virtually doped with Sn pre-included in the FTO substrate during annealing. Meanwhile, Nb(V) not only exists on the hematite surface as the oxide layer but also diffuses into the hematite in the annealing step, although it is drop-cast on pre-crystallized hematite. These thermally induced, counter-directional diffusions of Sn (upward diffusion) and Nb (downward diffusion) make the evaluation of modified hematite complicated, and require careful material design and cautious evaluation of its performance.

Acknowledgements

The authors thank the Global Frontier R&D Program on Center for Multiscale Energy System (2011-0031571) and the Korea Cen-

ter for Artificial Photosynthesis (KCAP) (No. 2009-0093880) funded by the Korea government (MSIP) through the National Research Foundation of Korea (NRF). H.P. is grateful to the Korea CCS R&D Center (KCRC) (No. 2014M1A8A1049354). This work was partially supported by the Qatar National Research Fund under its National Priorities Research Program (Award number NPRP 7-865-2-320).

Appendix A. Supplementary data

Supplementary data associated with this article can be found, in the online version, at <http://dx.doi.org/10.1016/j.apcatb.2016.08.059>.

References

- [1] R. van de Krol, M. Graetzel, Photoelectrochemical Hydrogen Production, Springer, New York, 2012.
- [2] K. Sivula, F. Le Formal, M. Gratzel, ChemSusChem 4 (2011) 432–449.
- [3] L. Vayssières, On Solar Hydrogen & Nanotechnology, John Wiley & Sons, Singapore, 2009.
- [4] G. Horowitz, J. Electroanal. Chem. 159 (1983) 421–436.
- [5] J.H. Kennedy, K.W. Frese, J. Electrochem. Soc. 125 (1978) 709–714.
- [6] A. Kleiman-Shwarsztejn, Y.S. Hu, A.J. Forman, G.D. Stucky, E.W. McFarland, J. Phys. Chem. C 112 (2008) 15900–15907.
- [7] G. Rahman, O.S. Joo, Mater. Chem. Phys. 140 (2013) 316–322.
- [8] A. Bak, S.K. Choi, H. Park, Bull. Korean Chem. Soc. 36 (2015) 1487–1494.
- [9] T. Hisatomi, F. Le Formal, M. Cornuz, J. Brillet, N. Tetreault, K. Sivula, M. Gratzel, Energy Environ. Sci. 4 (2011) 2512–2515.
- [10] R. Liu, Z. Zheng, J. Spurgeon, X.G. Yang, Energy Environ. Sci. 7 (2014) 2504–2517.
- [11] W. Kim, T. Tachikawa, D. Monllor-Satoca, H.I. Kim, T. Majima, W. Choi, Energy Environ. Sci. 6 (2013) 3732–3739.
- [12] J. Engel, H.L. Tuller, Phys. Chem. Chem. Phys. 16 (2014) 11374–11380.
- [13] A.G. Tamirat, W.N. Su, A.A. Dubale, H.M. Chen, B.J. Hwang, J. Mater. Chem. A 3 (2015) 5949–5961.
- [14] H.K. Dunn, J.M. Feckl, A. Mueller, D. Fattakhova-Rohlfing, S.G. Morehead, J. Roos, L.M. Peter, C. Scheu, T. Bein, Phys. Chem. Chem. Phys. 16 (2014) 24610–24620.
- [15] P.S. Shinde, A. Annamalai, J.H. Kim, S.H. Choi, J.S. Lee, J.S. Jang, Sol. Energy Mater. Sol. Cells 141 (2015) 71–79.
- [16] Y.C. Ling, G.M. Wang, D.A. Wheeler, J.Z. Zhang, Y. Li, Nano Lett. 11 (2011) 2119–2125.
- [17] H. Dotan, K. Sivula, M. Graetzel, A. Rothschild, S.C. Warren, Energy Environ. Sci. 4 (2011) 958–964.
- [18] F. Le Formal, N. Tetreault, M. Cornuz, T. Moehl, M. Gratzel, K. Sivula, Chem. Sci. 2 (2011) 737–743.
- [19] M. Wang, M. Pyeon, Y. Gonullu, A. Kaouk, S.H. Shen, L.J. Guo, S. Mathur, Nanoscale 7 (2015) 10094–10100.
- [20] L. Xi, S.Y. Chiam, W.F. Mak, P.D. Tran, J. Barber, S.C.J. Loo, L.H. Wong, Chem. Sci. 4 (2013) 164–169.
- [21] J.J. Deng, X.X. Lv, J.Y. Liu, H. Zhang, K.Q. Nie, C.H. Hong, J.O. Wang, X.H. Sun, J. Zhong, S.T. Lee, ACS Nano 9 (2015) 5348–5356.
- [22] X.L. Li, P.S. Bassi, P.P. Boix, Y.N. Fang, L.H. Wong, ACS Appl. Mater. Interfaces 7 (2015) 16960–16966.
- [23] R. Franking, L.S. Li, M.A. Lukowski, F. Meng, Y.Z. Tan, R.J. Hamers, S. Jin, Energy Environ. Sci. 6 (2013) 500–512.
- [24] K.S. Ahn, M.S. Kang, J.K. Lee, B.C. Shin, J.W. Lee, Appl. Phys. Lett. 89 (2006) 013103.
- [25] S.G. Chen, S. Chappel, Y. Diamant, A. Zaban, Chem. Mater. 13 (2001) 4629–4634.
- [26] H.N. Kim, J.H. Moon, ACS Appl. Mater. Interfaces 4 (2012) 5821–5825.
- [27] C. Sanchez, K.D. Sieber, G.A. Somorjai, J. Electroanal. Chem. 252 (1988) 269–290.
- [28] V.M. Aroutiounian, V.M. Arakelyan, G.E. Shahnazaryan, G.M. Stepanyan, E.A. Khachaturyan, H. Wang, J.A. Turner, Sol. Energy 80 (2006) 1098–1111.
- [29] Y.S. Hu, A. Kleiman-Shwarsztejn, A.J. Forman, D. Hazen, J.N. Park, E.W. McFarland, Mater. 20 (2008) 3803–3805.
- [30] R. Schrebl, K. Bello, F. Vera, P. Cury, E. Munoz, R. del Rio, H.G. Meier, R. Cordova, E.A. Dalchiele, Electrochim. Solid-State Lett. 9 (2006) C110–C113.
- [31] A. Kay, I. Cesar, M. Gratzel, J. Am. Chem. Soc. 128 (2006) 15714–15721.
- [32] D.K. Zhong, M. Cornuz, K. Sivula, M. Graetzel, D.R. Gamelin, Energy Environ. Sci. 4 (2011) 1759–1764.
- [33] U. Kang, H. Park, Appl. Catal. B 140 (2013) 233–240.
- [34] A. Bak, W. Choi, H. Park, Appl. Catal. B 110 (2011) 207–215.
- [35] V.M. Aroutiounian, V.M. Arakelyan, G.E. Shahnazaryan, H.R. Hovhannisyan, H. Wang, J.A. Turner, Sol. Energy 81 (2007) 1369–1376.
- [36] R. Morrish, M. Rahman, J.M.D. MacElroy, C.A. Wolden, ChemSusChem 4 (2011) 474–479.
- [37] Y.C. Ling, G.M. Wang, J. Reddy, C.C. Wang, J.Z. Zhang, Y. Li, Angew. Chem. Int. 51 (2012) 4074–4079.

- [38] X.H. Lu, Y.X. Zeng, M.H. Yu, T. Zhai, C.L. Liang, S.L. Xie, M.S. Balogun, Y.X. Tong, *Adv. Mater.* 26 (2014) 3148–3155.
- [39] M.H. Lee, J.H. Park, H.S. Han, H.J. Song, I.S. Cho, J.H. Noh, K.S. Hong, *Int. J. Hydrogen Energy* 39 (2014) 17501–17507.
- [40] P. Dias, T. Lopes, L. Andrade, A. Mendes, *J. Power Sources* 272 (2014) 567–580.
- [41] X. Zhang, H. Li, S. Wang, F.-R.F. Fan, A.J. Bard, *J. Phys. Chem. C* 118 (2014) 16842–16850.
- [42] J.Y. Kim, G. Magesh, D.H. Youn, J.W. Jang, J. Kubota, K. Domen, J.S. Lee, *Sci. Rep.* 3 (2013) 2681.
- [43] F.F. Abdi, N. Firet, R. van de Krol, *ChemCatChem* 5 (2013) 490–496.
- [44] H.W. Jeong, T.H. Jeon, J.S. Jang, W. Choi, H. Park, *J. Phys. Chem. C* 117 (2013) 9104–9112.